Technical University of Denmark

DTU

Flow analysis of vortex generators on wing sections by stereoscopic particle image velocimetry measurements

Velte, Clara Marika; Hansen, Martin Otto Laver; Cavar, Dalibor

DTU Library
Technical Information Center of Denmark

Flow analysis of vortex generators on wing sections by stereoscopic particle image velocimetry measurements

C M Velte, M O L Hansen and D Cavar

Technical University of Denmark, Department of Mechanical Engineering,
Fluid Mechanics Section, 2800 Kongens Lyngby, Denmark

E-mail: cve@mek.dtu.dk

Abstract
Stereoscopic particle image velocimetry measurements have been executed in a low speed wind tunnel in spanwise planes in the flow past a row of vortex generators, mounted on a bump in a fashion producing counter-rotating vortices. The measurement technique is a powerful tool which provides all three velocity components in the entire measurement plane. The objective of this study is to investigate the effect of vortex generators in a turbulent, separating, low Reynolds number ($Re = 20\,000$) boundary layer over a geometry which is generating an adverse pressure gradient similar to the flow past a wind turbine blade. The low Reynolds number is chosen on the basis that this is a fundamental investigation of the structures of the flow induced by vortex generators and the fact that one obtains a thicker boundary layer and larger structures evoked by the actuating devices, which are easier to measure and resolve. The flow behaves as expected, in the sense that the vortices transport high momentum fluid into the boundary layer, making it thinner and more resistant to the adverse pressure gradient with respect to separation. The amount of reversed flow is significantly reduced when vortex generators are applied. The idea behind the experiments is that the results will be offered for validation of modeling of the effect of vortex generators using various numerical codes. Initial large eddy simulation (LES) computations have been performed that show the same qualitative behaviour as in the experiments.

Keywords: vortex generators, separation control, stereoscopic PIV, LES

1. Introduction

Vortex generators (VGs), as described in [1], have been used for more than 50 years in applied aerodynamics on airplane wings. Vortex generators belong to the category boundary layer manipulators. Their function is to reenergize an adverse pressure gradient boundary layer that is about to separate by transporting high momentum fluid from the outer part of the boundary layer down to the low momentum zone closer to the wall. A vortex generator is commonly a small triangular or rectangular plate that is mounted on a surface at an angle to the incoming flow; see figure 1. A vortex generator acts like a small wing with a low aspect ratio, and the flow past the

tip creates a longitudinal vortex that convects high momentum fluid down into the boundary layer. The positive effect of vortex generators on an airplane wing is to delay separation to higher angles of attack, thus increasing the maximum lift coefficient so that an airplane can land at a lower speed. However, this increased maximum lift is paid for by a so-called drag penalty, where the drag for small angles of attack is increased. Vortex generators are also used to increase the maximum speed of commercial jets flying at approximately Mach 0.8. Locally on the wing, the flow is accelerated and can exceed the speed of sound, Mach 1, which can cause so-called shock induced separation even for very low angles of attack. This is easily felt by the pilot and determines the speed
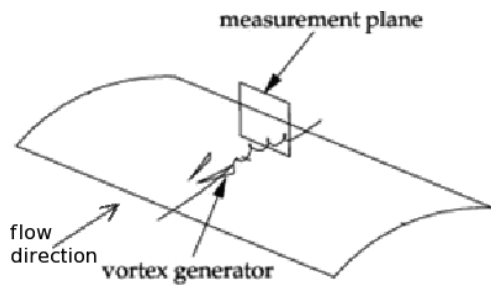
Figure 1. Triangularly shaped vortex generators.

Figure 2. (a) Counter-rotating and (b) co-rotating vortices.

limit on many subsonic passenger airplanes. However, vortex generators can also be used to delay this type of separation to allow the airplane to fly slightly faster. Since commercial jets have no problems in increasing the lift coefficient at for example landing configuration by using flaps and slats, the main reason that they often are equipped with vortex generators is shock induced separation.

For small airplanes and wind turbines, the flow is far from reaching Mach 1, and there is thus no problem with shock induced separation. However, sometimes a high lift coefficient is needed to decrease the landing speed for STOL (short take off and landing) airplanes. A classical solution has been to use so-called slots in front of the leading edge. The slot is a small, stationary list in front of the leading edge of the main wing that for large angles of attack allows high momentum flow from the pressure side to be accelerated in the slot between the list and the main wing, creating a high momentum flow to the suction side of the wing and thus making the flow more resistant to the adverse pressure gradient. Vortex generators have the same effect on the flow in the sense that they also delay separation and increase the maximum lift coefficient. Because they can be mounted/glued directly to the pressure side of a bare wing, a less complicated wing can be built, and therefore they are often used on modern sport planes instead of slots. Vortex generators are sometimes used to prevent separation of the flow past the rudder or ailerons to improve the controlling of the airplane, which could otherwise be drastically worsened. Vortex generators are used on wind turbine blades for two reasons. One is to decrease separation and increase lift at high angles of attack and the other is to attempt to increase the maximum ratio between the lift and the drag coefficients, which directly influences the aerodynamic efficiency of the turbine. The relative wind seen by a wind turbine blade is composed by the incoming wind speed and the rotational velocity of the blade. There exists an optimum value for the tip speed ratio, $\lambda_{opt} = \omega R / V_o$, where the wind turbine operates most efficiently. To run the turbine at this optimum value, it is necessary to increase the angular velocity of the rotor, ω, proportionally to an increasing wind speed, V_o. However, there is for noise reasons a limit on the speed of the tip of approximately 70 m s^{-1}, that gives a limit on the rotational speed of $\omega_{max} = 70/R$, where R is the rotor radius. The rotational speed of approximately 70 m s^{-1} at the tip decreases linearly further inboard with the decreasing radius. Thus, the flow at the tip will mainly be in the rotor plane, and near the hub the flow seen by the blade will almost be perpendicular to the
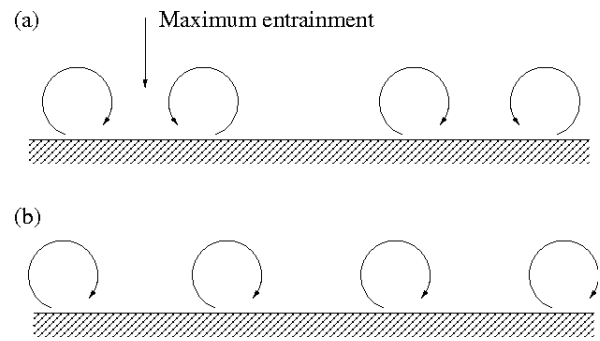
rotor plane. This twisting of the relative wind speed could in principle be compensated for by twisting the blades, but there is, for structural reasons, a limit to the extent to which this can be done. Since the relative wind speed increases towards the tip, the highest aerodynamic loads are also situated here, giving large bending moments at the root of the blades. To be able to carry these loads, the blade must be very thick close to the root, and eventually it often ends with a cylindrical cross section. The last real airfoil (i.e., with cross section with a sharp trailing edge) often has a thickness to chord ratio of more than 30%. This is very bad from an aerodynamic point of view in the sense that the flow may separate even for very small angles of attack. This, in combination with the fact that the angles of attack for these inboard sections, for the reasons given above, are large, almost guaranties a separated flow for all wind speeds even for pitch regulated machines. Since vortex generators are known to delay and to some extent suppress separation, it is natural to apply vortex generators on the inner part of wind turbine blades. Because vortex generators give some drag penalty also for low angles of attack, they are normally not used on the outer part of wind turbine blades. The fact that vortex generators can have quite a dramatic effect on the performance of wind turbines is shown in [2], where a comparison between the measured power curve on the 1 MW experimental *Avedøre* wind turbine is shown with and without vortex generators on the inner part of the blades. The maximum power occurring at a wind speed of around 17 m s^{-1} for a pitch of $-1°$ for the wind turbine running in stall regulation is approximately 850 kW for the clean configuration and 1050 kW when using vortex generators.

To have an effect over a section of a blade, vortex generators are mounted in arrays and often in pairs that can produce either co- or counter-rotating vortices; see figure 2. Also, the size, geometry, aspect ratio, angle of incidence to the flow, chordwise position in relation to the separation line, configuration of co- or counter-rotating vortices etc are parameters that must be optimized in order to use vortex generators in a most efficient manner.

In order to find these optimal parameters, one needs to do experiments. In [3] a review of many experiments and their conclusions made by Lin *et al* is given. In a recent paper by Godard and Stanislas [4], a parametric study of the effect of vortex generators was conducted in which the devices were placed on a bump designed to keep the boundary layer flow
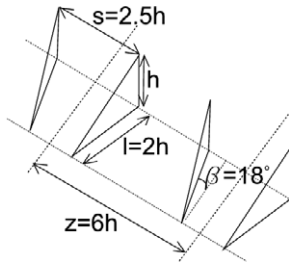
Figure 3. Sketch of vortex generator geometry.

on the verge of separation. An optimum vortex generator geometry was sought using hot film sensor skin friction measurements and thereafter characterized using stereoscopic particle image velocimetry (PIV). The main conclusions were that triangular vanes in a counter-rotating configuration give the best effect on skin friction increment. The optimal device configuration showed good concurrence with results found in the literature for all parameters except for the device height, which appeared to behave differently from results found in the literature. The characterization study done on the most optimal case showed counter-rotating vortices, stable in their downstream development, transferring momentum from the outer flow and in towards the near-wall region. In a recent study by Angele and Grewe [5], some experimental results on wind tunnel experiments using stereoscopic PIV on the flow past vortex generators are discussed, focusing on both the mean and instantaneous behaviour of the flow induced by the devices. The test section consisted of a concentric inner cylinder ending in a cone made of wire gauze, through which suction was applied, creating an adverse pressure gradient. A center body was in turn placed downstream of this cone to generate a favorable pressure gradient. The vortex generators succeeded in obstructing the separation created by the adverse pressure gradient. It was also found that the vortices were nonstationary, with larger movements in the spanwise direction than in the wall normal one. The spanwise movements were of the same extent as the size of the vortices.

In an ongoing research project, the flow field behind different vortex generators mounted on top of a cylindrical bump was investigated experimentally. The purpose is to create a database that can be used for validating various numerical codes to correctly calculate the physics contained in the production of the vortices and their dynamic behaviour embedded in the viscous boundary layer. Some of the results obtained so far are given in this paper.

2. Method

2.1. Wind tunnel setup

The measurements were carried out in a closed-circuit wind tunnel with an 8:1 contraction ratio and a test section of cross sectional area 300 mm × 600 mm with length 2 m. The suction side of a wind turbine wing is represented by a bump mounted vertically on one of the test section walls with the leading edge positioned 600 mm downstream of the inlet grid. The bump is

a circular sector, extended in the spanwise direction, creating a cylindrical sector with radius 390 mm. The bump height is 30 mm and the chord length and bump width are 300 mm and 600 mm respectively. The presence of this model in the flow induces an adverse pressure gradient strong enough to generate separation. The experiments were conducted at a free stream velocity of $U_\infty = 1$ m s^{-1}, corresponding to Reynolds number $Re = 20\,000$ based on the bump chord length. The turbulent inflow is assured by a turbulence generating inlet grid with mesh length $M = 39$ mm situated at the beginning of the test section. In [6], the turbulence intensity at the inlet has been estimated to 12% and the boundary layer thickness at the vortex generator position has been estimated from laser Doppler anemometry (LDA) measurements to be 25 mm.

The boundary layer is here defined as the part of the flow contained by vorticity derived from the presence of the wall. The principle of determining the boundary layer thickness is to determine where the vorticity is reduced to a value much smaller than the maximum value ($\omega_z = 0.01\,\omega_{z\,\text{max}}$). This is here defined as the boundary where the viscous effects cease to influence the flow. When calculating the vorticity, it is tedious to do measurements that give you the data to calculate both terms. In the potential flow free stream, the first term and the second term must cancel out since there is no vorticity. In the boundary layer, however, vorticity is present, which means that the terms must be unequal. An order of magnitude analysis gives that if U and x are of order 1, then V and y are of order δ. Therefore the second term is quadratically larger than the first term.

$$\omega_z = \frac{1}{2}\left(\underbrace{\frac{\partial V}{\partial x}}_{\frac{\delta}{1}} - \underbrace{\frac{\partial U}{\partial y}}_{\frac{1}{\delta}} \right). \tag{1}$$

Therefore one can argue that the second term should be sufficient in determining the vorticity. The boundary layer thickness was therefore extracted from a velocity profile measured by LDA at the position of the trailing edges of the vortex generators with no actuators present. $\partial U/\partial y$ was obtained from the velocity profile and thereby also the estimate of the vorticity.

2.2. Actuators

Triangular vanes of the same height as the boundary layer thickness, 1δ, were applied. δ represents the boundary layer thickness at the position of the trailing edges of the devices. The vortex generators were positioned with their trailing edges at 50% bump chord. The resulting parameters from the optimal vortex generator configuration found as a result of the optimization study performed by Godard and Stanislas [4] have been used and can be found in figure 3, where h is the device height, l is the device length, s is the distance between the trailing edges of two vortex generators within one pair, z is the distance between two vortex generator pairs and β is the device angle of incidence. This optimum geometry will, of course, depend on the application and is therefore most likely not universal, but has nevertheless also been used in this experiment. The distance between the devices and the separation line showed a weak dependence on the wall shear stress and was therefore not considered in this study.
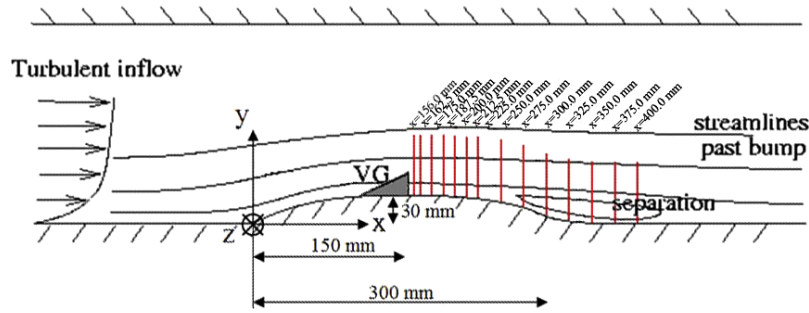
Figure 4. Sketch of the wind tunnel test section, the positioning of measurement planes and definition of coordinate system.

2.3. Measurement planes

The measurements were conducted in spanwise planes at various positions downstream of the vortex generators. A sketch of the wind tunnel test section and the positioning of measurement planes is shown in figure 4, where also the coordinate system is defined. The equipment was mounted on a rigid traverse, traversing in the axial and normal directions. This configuration enables one to calibrate only once and perform measurements accurately at the different streamwise positions using the same calibrated configuration. All measurement planes are parallel to each other, and their normal component is parallel to the test section walls.

2.4. Setup of stereoscopic PIV (SPIV) equipment

The experimental setup is illustrated by a sketch in figure 5. A laser was placed at the top of the test section, illuminating the vertically mounted bump from the side. Two cameras were placed on the same side of the light sheet, resulting in one camera being placed in the forward scattering direction and one in the backward scattering one. The angle of each respective camera to the laser sheet was 45°. The f-numbers were set to between 8 and 16 for the camera in the forward scattering direction and 4 or 5.6 for the camera in the backward scattering direction, depending on the light budget of reflections from the particles and the bump and devices at each individual plane position. The stereoscopic PIV equipment included a double cavity NewWave Solo 120XT Nd-YAG laser (wavelength 532 nm), capable of delivering light pulses of 120 mJ. The pulse width, i.e., the duration of each illumination pulse, was 10 ns. The light sheet thickness at the measurement position was 2 mm and was created using a combination of a spherical convex and a cylindrical concave lens. The equipment also included two Dantec Dynamics HiSense MkII cameras (1344 × 1024 pixels) equipped with 60 mm lenses and filters designed to only pass light with wavelengths close to that of the laser light. Both cameras were mounted on Scheimpflug angle adjustable mountings. In order to obtain a smaller measurement area, the cameras were, in some of the tests, equipped with teleconverters. The seeding, consisting of glycerol droplets with a diameter of 2–3 μm, was added to the flow downstream of the test section. The seed particles were added at this position in order to obtain a more homogeneous distribution of the tracers throughout
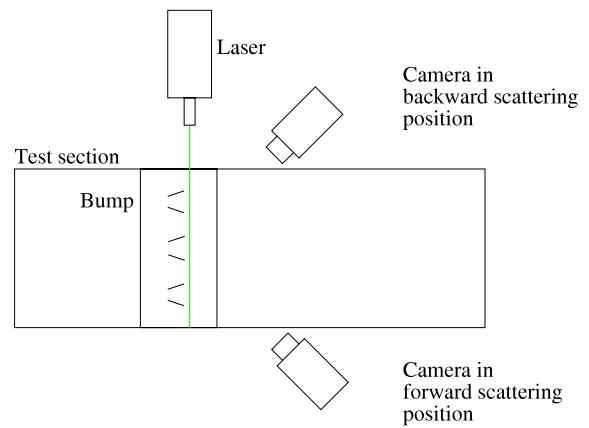

Figure 5. Sketch of the SPIV setup at the test section.

the measurement volume without significantly disturbing the flow. This kind of global seeding of the complete tunnel is possible since the tunnel is a closed-circuit wind tunnel. The size of the seed particles has been measured by an APS TSI 3320 time-of-flight spectrometer. The droplets are produced by blowing pressurized air over a thin-walled pipe with diameter of 0.5 mm. The other end of the pipe is submerged in glycerol.

A calibration target was aligned with the laser sheet. This target has a well defined pattern, which can be registered by the two cameras to obtain the geometrical information required for reconstructing the velocity vectors received from each camera to obtain a full description of all three velocity components in the plane. Calibration images were recorded with both cameras at five well defined streamwise positions throughout the laser sheet. A linear transform was applied to these images for each camera respectively to perform the reconstruction. This procedure was executed both previous to and after the measurements.

2.5. Data processing

The images were processed using Dantec Flowmanager software version 4.7. Adaptive correlation was applied using refinement with an interrogation area size of 32 × 32 pixels. Local median validation was used in the immediate vicinity of each interrogation area to remove spurious vectors between each refinement step. The overlap between interrogation areas was 50%. For each measurement position, 500 realizations
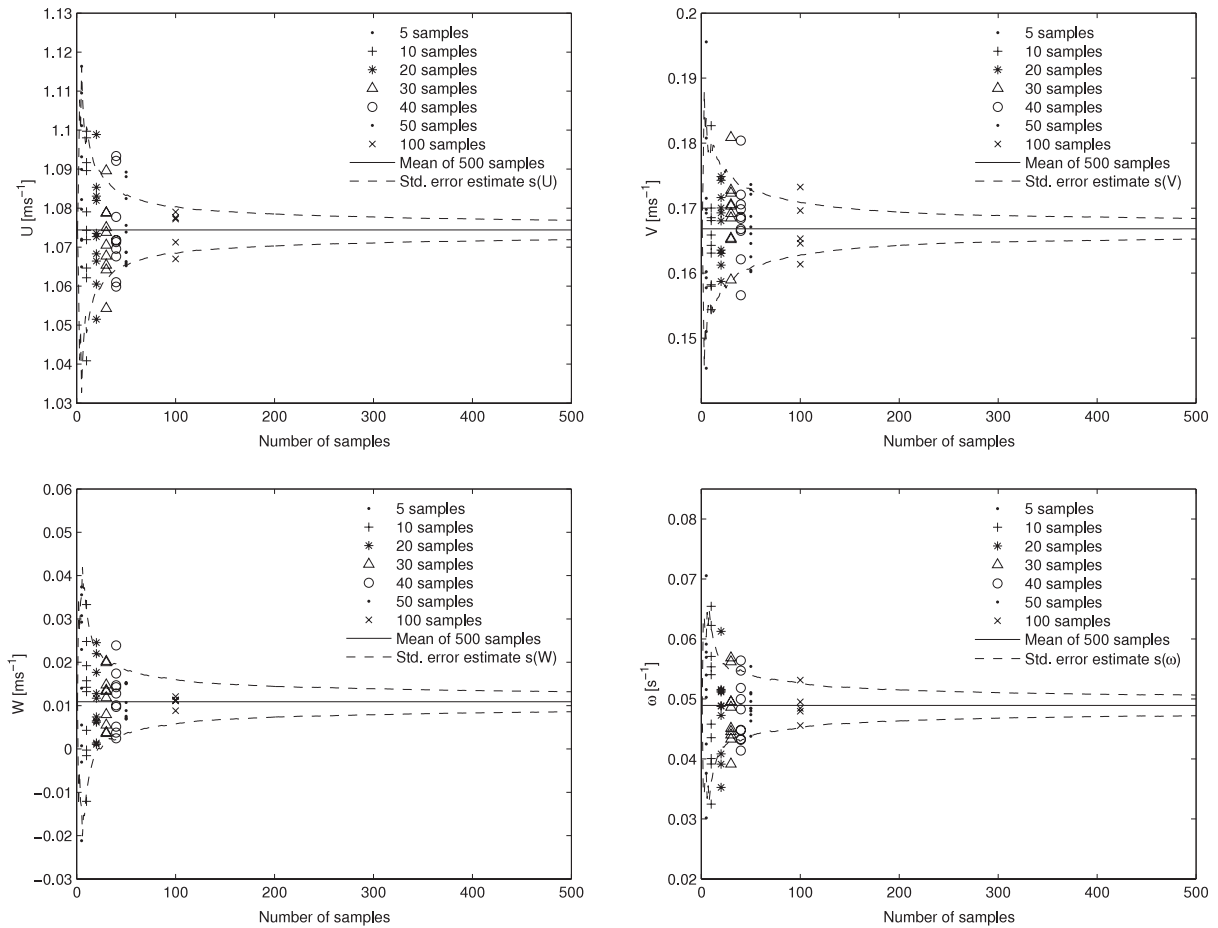
Figure 6. The effect of sample size on accuracy of $\overline{U}, \overline{V}, \overline{W}$ and $\overline{\omega}$ based on a single measurement point $(z/h, y/h) = (1, 1)$ in $N = 500$ vector maps ($\overline{(\cdot)}$ indicating average). Plotted points represent averages of the number of independent samples given in the figure. Additionally, 10 statistically independent averages based on 5, 10, 20, 30, 40 and 50 ensembles and 5 averages based on 100 ensembles are included in the figures.

were acquired. The recording of image maps was done with an acquisition rate of 1.0 Hz.

2.6. Mean fields, spatial resolution and accuracy

The velocity vector maps contain 73 by 63 vectors. The interrogation areas have linear dimensions 1.15 mm in the y-direction and 1.73 mm in the z-direction. In the PhD thesis of Schmidt [6], the Taylor microscale was estimated from LDA measurements of time series to be in the order of $\lambda_f \approx 9$ mm at a position 330 mm upstream of the bump leading edge at mid-channel. The estimate of the Kolmogorov length scale was in the order of $\eta \approx 0.5$ mm. LDA velocity profile measurements had also been used to obtain the wall shear stress at the same downstream position. From this an estimate of the viscous lengthscale is obtained, $\delta_\nu = \nu(\rho/\tau_w)^{1/2} = 0.2$ mm. The spatial resolution of the velocity vector fields is defined by the size of the interrogation area, which also limits the spatial resolution of the estimation of velocity gradients and hence the vorticity. In order to resolve the smallest scales in the flow, one needs to fulfill the Nyquist criterion. Therefore, scales smaller that half of the size of the interrogation area can not be resolved. Streamwise vorticity was calculated using central differencing, which gives second-order accuracy

of the velocity derivative estimate and half the uncertainty of for example the forward or backward difference. The scheme cancels out the effect of oversampling from the 50% overlap between interrogation areas, in the estimation of the velocity gradient, since neighboring data are not correlated (see e.g. Raffel *et al* [7]).

The effect of sample size on accuracy has been investigated in one single point $((z/h, y/h) = (1, 1), x = 225$ mm) for the first moment for the x-, y- and z-component of the velocity. The same has been done for the first moment of the vorticity. The results are shown in figure 6. The maximum number of realizations was $N = 500$. The mean based on this sample size is shown by a filled straight line. The dashed lines indicate the theoretical standard error estimates for the first moment.

$$s(U) = \frac{\sigma}{\sqrt{N}}. \tag{2}$$

Additionally, 10 statistically independent averages based on 5, 10, 20, 30, 40 and 50 ensembles and 5 averages based on 100 ensembles are included in the figures. The result does not vary significantly for other measurement points.

Since the PIV velocity measurement points are local averages over the area of interrogation, one can never obtain

Table 1. Control parameters for evaluation of correlation noise.

Control parameters	
$N_I \geqslant 10$–20	Particle image density
	N_I—mean number of particle images in an interrogation area
$F_O \geqslant 0.75$	Loss of particles due to out-of-plane motion
	F_O—fraction of particles present inside the interrogation area in both images
$M\|\Delta U\|\Delta t/d_\tau \leqslant 0.5$	Velocity gradients
	M (pix m^{-1})—image magnification
	ΔU (m s^{-1})—difference in velocity across the interrogation area
	Δt (s)—time between acquired PIV images
	d_τ—mean particle image diameter

measurements closer to the wall than half of the height of the interrogation area size. And even then, because of the high velocity gradients in this region, one needs to be careful in interpreting the measurements at these points. Therefore, the position of the wall was determined by extrapolating the mean velocity profiles towards the wall and using the no-slip condition.

Keane and Adrian [8] used an analytical model and Monte Carlo simulations to investigate the effects of experimental parameters to optimize PIV performance. They showed that double-pulsed systems were optimal when the interrogation area particle image density exceeded 10–20. They also showed that velocity gradients reduce the valid data rate and introduce velocity bias. The primary source of error in two-component PIV measurements is correlation noise. Westerweel [9] and Foucaut *et al* [10] have shown that if the values of the control parameters in table 1 are satisfied, then the root mean square (RMS) of the measured particle image displacements $\sigma_{corr} \approx 0.1$ pixel.

The dominating factor from table 1 is the effect of velocity gradients, which was only altered by changing the image magnification and the time between pulses. If there are large velocity gradients in the flow, variations of particle displacements across the interrogation areas will lead to a broadening of the correlation peak. This will in turn lead to deterioration in the precision of the estimate of the position of the correlation peak. If one lets the time separation between acquired images be relatively large, this precision error will be small in relation to the displacement. However, if velocity gradients are present, this strategy will also lead to a broadening of the correlation peak, since the variation in displacement will increase as the time separation increases. The choice of experimental design will therefore by necessity have to be a tradeoff between precision and relative displacement error. If the velocity gradients vary across the measurement plane, one cannot design the experiment so that it is optimized over the entire measurement volume. The number of spurious vectors was always less than 5%, which shows that the effect of large velocity gradients in the flow on accuracy was not unwieldy.

Since the main flow component is perpendicular to the measurement plane, the finite thickness of the laser sheet will be critical in limiting the dynamic velocity range, i.e., the ratio of the maximum velocity to the minimum resolvable velocity. Maximizing the dynamic velocity range

is of importance for accuracy issues, originating from the difficulties of determining the position of the particle image. A larger dynamic range will minimize the effect of this uncertainty. Therefore, the measurements need to be a tradeoff between the laser sheet thickness and the time between laser pulses.

Another source of error, which is not commonly considered, is the ability of the particles to follow the flow. This might be an issue, especially in regions of accelerating flow such as in a large scale rotation. An example of this in the longitudinal vortices behind vortex generators. Due to the excess density of the particles in relation to the surrounding medium, there is a centrifugal force acting on them, forcing them to move outwards from the vortex center. This is however discarded from having any significant effect in the flow under consideration because of two reasons: the velocities are very low and the distribution of particles in the PIV images is homogeneous. At higher velocities, a reduced particle concentration in the vortex core is commonly observed (see e.g. Stanislas *et al* [11]).

2.7. Reflection reduction

Reflections from vortex generators and bump surface entering the CCD cameras constituted a problem for two reasons. The reflections appeared in the most interesting part of the measurement region, corrupting the signal in this area. The high power of the laser light also creates reflections harmful for the CCD chip. If these high power reflections reach the CCD chip, one is risking damage to the cameras in the form of dead pixel elements. Light scattering from objects other than the glycerine particles was removed by painting the reflecting surfaces with a mixture of Rhodamine 6G and varnish. Rhodamine 6G is a fluorescent dye, absorbing light with the wavelength of the laser and reflecting light which has a wavelength slightly shifted from the absorbed one. The cameras were equipped with green-pass filters, which only permit the wavelengths of the laser to pass, allowing the scattering from the particles to pass through and preventing strong reflections from surfaces to reach the CCD chip. Rhodamine 6G has its absorption peak at around 530 nm and its emission peak at about 552 nm. This method was successful in reducing most of the unwanted reflections. An additional approach used in some of the measurement positions was to take pictures with no particles present in the flow at

the same position as that at which the measurements were taken. These pictures were subtracted from the images used for measurements prior to processing, removing scattering from all objects other than the particles.

Before applying Rhodamine 6G, acquiring images including the wall and receiving a good quality measurement signal was not possible since, even at relatively low laser intensity, the reflections from the wall were too strong, risking damage to the CCD chip. The effect of applying Rhodamine 6G to the bump surface made measurements with maximum laser power close to the surface possible for all measurement positions. The largest reflection reducing effect is, however, obtained by utilizing the reflection subtraction technique, removing almost all of the reflections from the wall and in particular the reflections from the vortex generators as close up as 6 mm from the device trailing edges. Previous to applying this technique, reflections from the vortex generators obstructing the signal were detected as far as up to 100 mm downstream of the devices.

2.8. Large eddy simulation (LES) computations

The eddy–viscosity based LES calculations were performed utilizing the flow solver **FASTEST-3D** (flow analysis solving transport equations simulating turbulence), [12]. The code is based on a finite-volume numerical method for solving both three-dimensional filtered and Reynolds-averaged Navier–Stokes equations on block-structured, body-fitted, non-orthogonal meshes. Block interfaces are treated in a conservative manner, consistent with the treatment of inner cell faces. A cell-centered (collocated) variable arrangement and Cartesian vector and tensor components are used. The well-known SIMPLE algorithm is applied for coupling the velocity and pressure fields. The convective and diffusive transport of all variables is discretized by a second-order central differencing scheme, whose stability is enhanced through the so-called deferred correction approach. Time discretization is accomplished by applying the second-order implicit Crank–Nicolson method. FASTEST-3D is parallelized based on domain decomposition in space using the MPI message passing library.

The computational setup regarded in LES calculations is somewhat different from the experimental one. The same geometrical bump is considered, with vortex generators placed at the same positions as in the experiment; see figure 3. As the FASTEST code utilizes block-structured meshes, a trapezoidally shaped vortex generator pair is used in the numerical setup in order to avoid grid discontinuity at the leading edge of the vortex generator vanes. Therefore, the leading edge of the vortex generator pair has a height of $1/5\delta$, while the trailing edge height corresponds to the value applied in the experiments (1δ). It should also be noted that the inlet conditions in the conducted LES computations do not match the experimental counterpart, as precomputed snapshots of the spatially developing fully turbulent boundary layer flow are used as an inlet database for the computations, and only one device pair is considered in the computations. The computational domain considered consists of a cross-sectional area of 240 mm × 288 mm in the wall normal and

spanwise directions respectively (300 mm × 600 mm in the experiment) and a total length in the streamwise direction of 1.2 m, where 300 mm upstream of the bump leading edge and 600 mm downstream of the bump trailing edge are included in the domain. In the spanwise direction, periodic boundary conditions (BCs) are applied, while in the wall normal direction the solid wall (bottom bump surface) and symmetry boundary conditions (upper domain surface) are applied. Note that the upper wall boundary layer is not included in the computations. Additionally the inlet and (convective) outlet BCs are applied in the streamwise direction. Vortex generators are modeled as '*baffles*' i.e., surfaces without thickness with wall BCs applied to them. The choices of boundary conditions and domain dimensions are largely connected to the inlet inflow database used in the computations. The inlet database representing the instantaneous snapshots of a fully developed turbulent boundary layer flow was generated on a precursor basis using the method of [13]. In the recent work of [14], the LDA measurements of the fully developed boundary layer flow past a 2D bump without vortex generators mounted on it are reasonably well reproduced by LES. Using the same inlet database and very similar geometrical and numerical computational layout as in [14], the present LES computation is conducted.

The subgrid-scale (SGS) stresses are modeled using the eddy–viscosity assumption employing the Smagorinsky model [15]. The grid consists of 584 × 162 × 224 ($\approx$21.3 million) cells in the streamwise, wall normal and spanwise directions respectively. Special consideration has been made to obtain the proper mesh resolution in the area of the vortex generators. Approximately 3.8 million cells are located in the immediate vicinity of the vortex generators, potentially facilitating the computations with the possibility to properly resolve various turbulent and vortical structures in this area.

3. Results and discussion

3.1. Downstream development of vortices

In order to be able to quantify the induced effect of the vortex generators on the flow, both the controlled and the uncontrolled flow has been measured for all positions. In figure 7, for four positions downstream of the streamwise placement of the vortex generators, the arithmetic averages of the velocity vector maps obtained from SPIV measurements of the uncontrolled (left column) and controlled (middle column) flows are displayed. The estimator of the mean is based on 500 recorded independent velocity field realizations. The rightmost column shows the projected longitudinal vorticity of each corresponding mean velocity vector map for the controlled case. In the left and middle columns, the secondary velocities are illustrated as arrows, whereas the primary velocities are plotted as colour contours. For the sake of clarity, only every fourth vector has been displayed in these plots, but the data in the contour plots have not been reduced. The positions of the planes are given in absolute coordinates, referring to the coordinate system given in figure 4, as well as in coordinates relative to the vortex generators. The *y*-coordinate is always
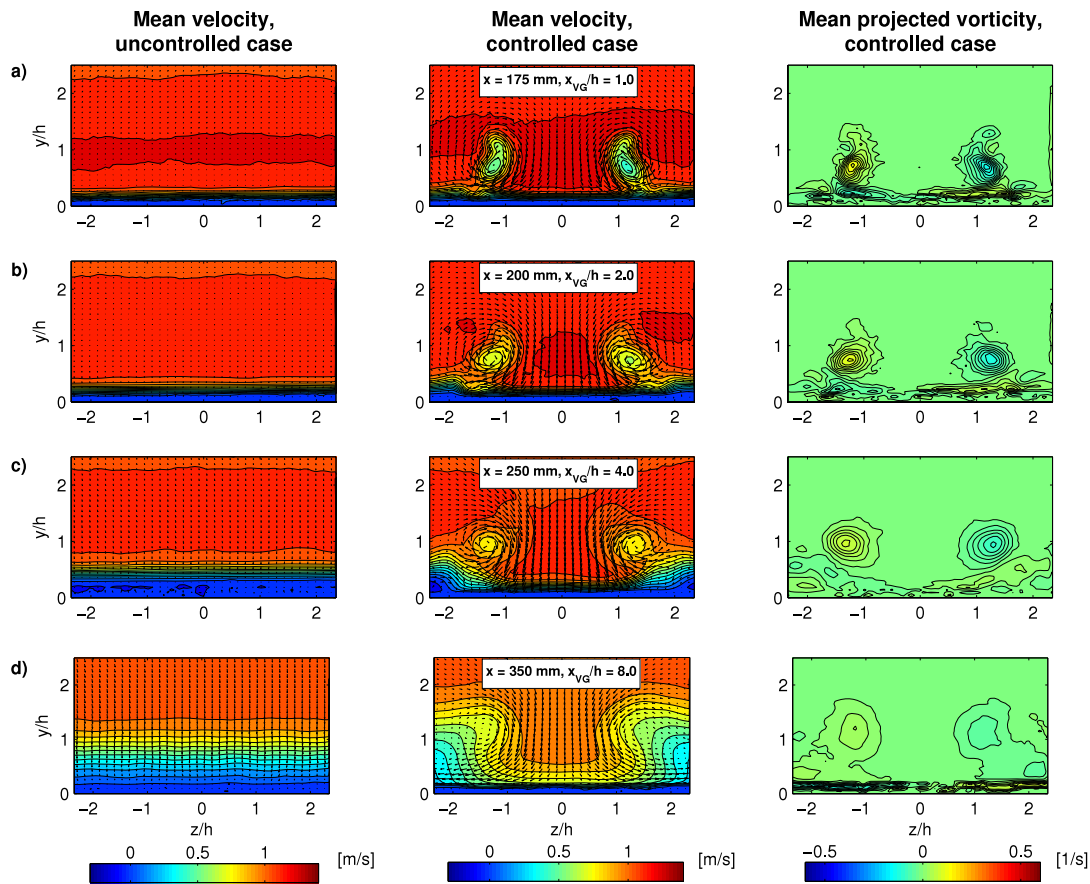
Figure 7. Plots of averaged velocity fields. The left column displays the uncontrolled case, the middle column shows the corresponding controlled case and the right column displays the corresponding projected longitudinal vorticity for the controlled case, represented by contours. In the velocity vector plots, the in-plane components are represented by vectors and the out-of-plane component is represented by contours. These quantities are displayed for four positions downstream of the vortex generators ((a) $x_{VG}/h = 1$, (b) $x_{VG}/h = 2$, (c) $x_{VG}/h = 4$ and (d) $x_{VG}/h = 8$), $h/\delta = 1$, showing the streamwise development of the flow field. The largest secondary velocities are of the order of 0.5 m s^{-1}, which can be compared to the free stream velocity of approximately $U = 1$ m s^{-1}.

zero at the wall surface. The four downstream positions of the measurement planes are $x_{VG}/h = 1, 2, 4$ and 8, where x_{VG} has the same direction as the x-component, with its origin at mid chord of the bump (at the trailing edges of the devices), i.e., $x_{VG} = 0$ at $x = 150$ mm.

It can be seen in the velocity fields in figure 7 that the uncontrolled flow displays a 2D boundary layer, experiencing separation in the area around the bump trailing edge. One can also see that the vortex generators have a quite substantial impact on the boundary layer. The presence of the vortex generators causes the flow to rotate, creating counter-rotating longitudinal vortices distorting the flow so that the high momentum fluid is transported from the outer flow into the near-wall region in the downwash region (in the vicinity of $z = 0$). The boundary layer becomes significantly thinner in this zone, whereas the low momentum fluid is transported upwards in the upwash region between two vortices as seen on the sides in the velocity plots. One can also see the downstream development of the flow field, where the vortices start off more or less isolated from effects due to the wall. The vortices are then gradually integrated with the remaining part of the boundary layer flow, eventually submerging into the boundary layer. The vorticity plots reveal that the vortex

generators on average give rise to primary vortices, which in turn generate shear layers due to the presence of the wall. One can also see that, throughout the downstream development of the longitudinal vortices, the mean distance between the vortices is almost constant. This distance is close to the distance between the trailing edges of two vortex generators within one pair. The mean of the longitudinal vortices therefore does not move substantially in the spanwise direction. One can also see a progression of the vortices away from the wall as one moves through the downstream direction, which is expected from inviscid theory.

The induced effect of the vortex generators on the boundary layer can also be seen in figure 8, which shows the estimated mean of the measured axial and normal velocity profiles at different streamwise positions in the controlled and uncontrolled configuration in the symmetry plane, situated in the downwash region ($z = 0$ mm). It is clearly seen that the transfer of high momentum into the boundary layer from the vortex generators decreases the separation behind the bump at this spanwise position. The increase in downwash due to the vortex generators can be seen in the normal velocity profiles in figure 8(b) and the effect on the reduction of recirculating flow can accordingly be traced in figure 8(a).
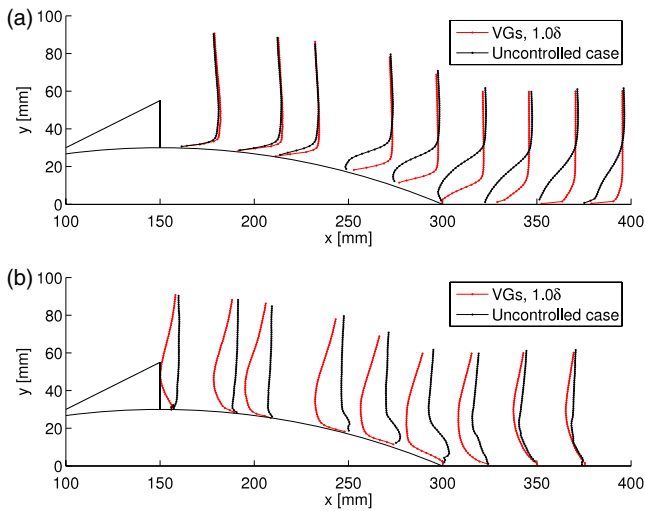
Figure 8. Streamwise (a) and normal (b) velocities in the downwash region ($z = 0$). The normal velocity has been scaled with a factor of four compared to the streamwise one.

Figure 9. Reversed volumetric flow rate for every measurement position normalized by the total flow rate in each respective measurement plane.

3.2. Volumetric flow rate

The volumetric flow rate has been calculated by integrating the streamwise velocity component, U, for each vector over its respective interrogation area and summing all of these values up for each respective measurement plane. By performing this calculation for all axial vector components that are negative in the streamwise direction, one obtains an estimate of the reversed flow rate. Figure 9 shows the magnitude of the reversed volumetric flow rate calculated from the estimator of the mean for the controlled and the uncontrolled case. This flow rate has been non-dimensionalized with the total flow rate through each respective measurement plane, i.e., the volumetric flow rate for both the negative and the positive streamwise vectors have been included. The plot thus shows the streamwise development of the separation for the two cases with and without devices. One can clearly see that the vortex generators reduce the amount of reversed volumetric flow rate substantially. However, they do not eliminate the backflow. The largest backflow in the clean case is found at measurement position $x = 300$ mm, which can be explained from the discontinuity in the geometry in the model at the border between the trailing edge of the bump and the test section wall. At $x = 300$ mm, the reduction in the normalized reversed flow rate is 89% of the case without vortex generators. The unsteady point of separation, which on average is located at a streamwise position of approximately $x = 210$ mm (known from [6]), is not substantially affected by the vortex generators; however, it is evident that the reattachment point at $x = 350$ mm (also known from [6]) is significantly affected by the vortex generators.

3.3. Vortex generator modeling

Figure 10 shows the time averaged velocity fields of the SPIV measurements (left column) and the LES simulations (right column) for four planes ($x = 175, 200, 250$ and 350 mm) for
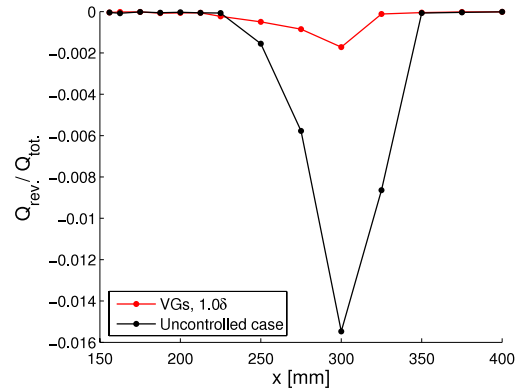
triangular vanes of height $h/\delta = 1.0$. The planes correspond to positions within and in the vicinity of the separation region in the clean configuration. One can see that the longitudinal vortices have the same qualitative structure and downstream development in the measurements and the computations. It is seen that LES has the ability of capturing similar large scale structures in the flow due to the effect of the vortex generators as observed from the PIV measurements. The vortices start out as isolated vortices and gradually submerge into and unite with the boundary layer further downstream. However, one can see that the agreement is not perfect and it is not possible to make a direct comparison since the geometry and inlet conditions used in the experiments are not exactly identical to the ones used in the computations. Still, the concurrence between the measurements and the computations shows that the sensitivity in modeling to geometry of this flow by LES is not high for this particular case. Beyond these matters, a perfect agreement is still not expected. Inherent assumptions in the computations also give rise to non-correspondence between measurements and modeling. LES assumes that the boundary layer flow obeys the log law and that there exists an inertial subrange, independently of the Reynolds number. It has been shown from experiments, [16], that the Reynolds-stress profiles in the overlap region depend on the Reynolds number. Therefore the turbulent processes can not be completely independent of Reynolds number, and the boundary layer flow predicted by LES will never concur completely with experiments because of the low Reynolds numbers.

4. Conclusions

It has been shown that it is possible to measure and resolve the flow created by a row of vortex generator pairs inducing counter-rotating vortices and their effect on the boundary layer using SPIV. It is apparent from the results that the vortex generators have the expected effect on the flow in the sense that they create large scale mixing near the wall. The measurements clearly show a structured vortex behind each vortex generator, whose development can be traced throughout the downstream planes. The effect of the vortex generators on the amount
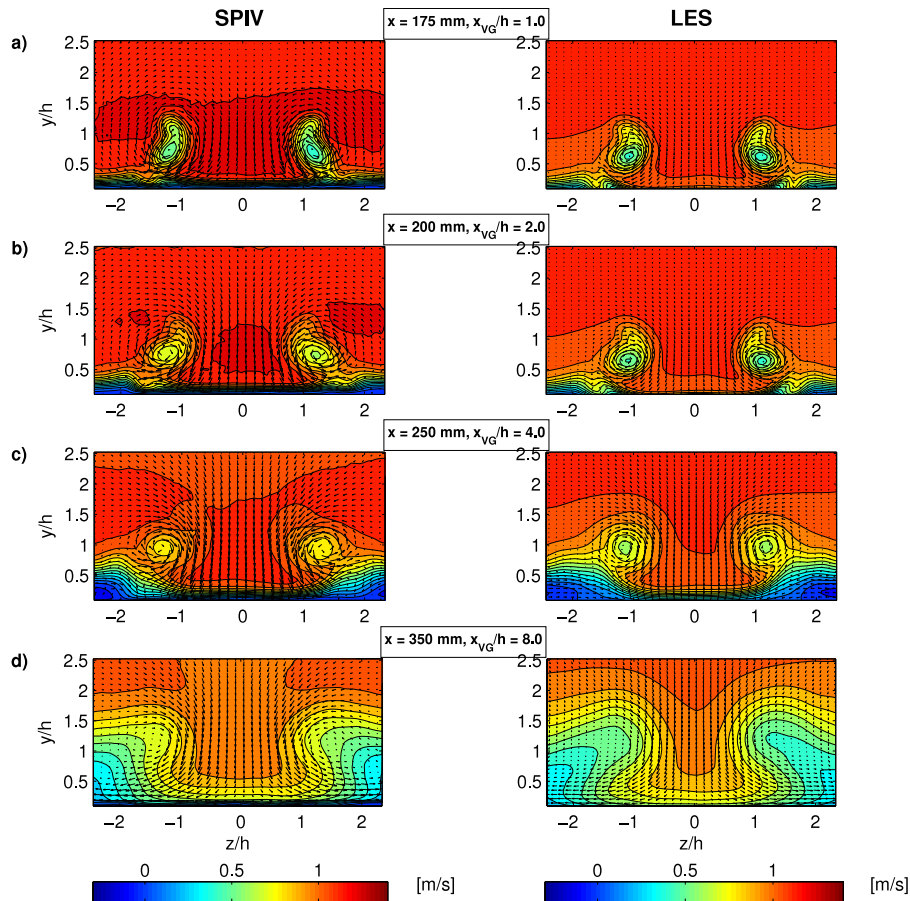
Figure 10. Plots of averaged velocity fields with in-plane components represented by vectors and out-of-plane component represented by contours for four positions downstream of the vortex generators ((a) $x_{VG}/h = 1$, (b) $x_{VG}/h = 2$, (c) $x_{VG}/h = 4$ and (d) $x_{VG}/h = 8$), $h/\delta = 1$. The left column shows results from SPIV measurements and the right column shows corresponding results from large eddy simulation (LES). The largest secondary velocities are of the order of 0.5 m s^{-1}, which can be compared to the free stream velocity of approximately $U = 1$ m s^{-1}.

of reversed flow is significant and shows a clear reduction in the amount of recirculation. The separation point seems not to be substantially affected, whereas the reattachment point is influenced, curtailing the extent of the separated region. The expected behaviour of the streamwise and normal velocities in the downwash region was observed.

A qualitative comparison with LES simulations of a slightly different case of the flow behind vortex generators shows that LES is capable of reproducing the overall flow structure. LES has the ability of capturing the large scale structures in the flow induced by the vortex generators. Previous tests with Reynolds-averaged Navier–Stokes (RANS) models have shown not to possess this capability for the case under consideration. In the future these measurements will be used to further validate various numerical methods for calculating the flow behind vortex generators.

Acknowledgment

References

[1] Taylor H D 1947 The elimination of diffuser separation by vortex generators *United Aircraft Corp. Report No.* R-4012-3
[2] Øye S 1995 The effect of vortex generators on the performance of the ELKRAFT 1000 kW turbine *9th IEA Symp. Aerodynamics of Wind Turbines* (*Stockholm*) ISSN 0590-8809
[3] Lin J C 2002 Review of research on low-profile vortex generators to control boundary-layer separation *Prog. Aerosp. Sci.* **38** 389–420
[4] Godard G and Stanislas M 2006 Control of a decelerating boundary layer. Part 1: optimization of passive vortex generators *Aerosp. Sci. Technol.* **10** 181–91
[5] Angele K P and Grewe F 2007 Instantaneous behavior of streamwise vortices for turbulent boundary layer separation control *J. Fluids Eng.* **129** 226–35
[6] Schmidt J J 1997 Experimental and numerical investigation of separated flows *PhD Thesis* Department of Mechanical Engineering ET-PHD 97-01, MEK-DTU
[7] Raffel M, Willert C and Kompenhans J 1998 *Particle Image Velocimetry—A Practical Guide* 3rd printing (Berlin: Springer)
[8] Keane R D and Adrian R J 1990 Optimization of particle image velocimeters. Part I: double pulsed systems *Meas. Sci. Technol.* **1** 1202–15

[9] Westerweel J 2000 Theoretical analysis of the measurement precision in particle image velocimetry *Exp. Fluids* **29** S3–12

[10] Foucaut J, Miliat B, Perenne N and Stanislas M 2004 Characterization of different PIV algorithms using the EUROPIV synthetic image generator and real images from a turbulent boundary layer *Particle Image Velocimetry: Recent Improvement. Proc. EUROPIV 2 Workshop on Particle Image Velocimetry (Zaragoza, March–April 2003)* ed M Stanislas *et al* (Berlin: Springer)

[11] Stanislas M, Okamoto K and Khler C 2003 Main results of the first Int. PIV challenge *Meas. Sci. Technol.* **14** R63–89

[12] Durst F and Schafer M 1996 A parallel block-structured multigrid method for the prediction of incompressible flows *Int. J. Numer. Methods Fluids* **22** 549–65

[13] Lund T S, Xiaohua W and Squires K D 1998 Generation of turbulent inflow data for spatially-developing boundary layer simulations *J. Comput. Phys.* **140** 233–58

[14] Cavar D 2006 Large eddy simulation of industrially relevant flows *PhD Thesis* Department of Mechanical Engineering MEK-FM-PHD 2006-02, MEK-DTU

[15] Smagorinsky J 1963 General circulation experiments with the primitive equations *Mon. Weather Rev.* **91** 99–165

[16] Gad-el-Hak M and Bandyopadhyay P R 1994 Reynolds number effects in wall-bounded turbulent flows *Appl. Mech. Rev.* **47** 307–65